The Meteoritical Society

Meteoritics & Planetary Science 48, Nr 9, 1572–1589 (2013)
doi: 10.1111/maps.12183

Grove Mountains 020090 enriched lherzolitic shergottite: A two-stage formation model

Yangting LIN[1*], Sen HU[1], Bingkui MIAO[2], Lin XU[3], Yu LIU[1], Liewen XIE[1], Lu FENG[1], and Jing YANG[1]

[1]Key Laboratory of the Earth's Deep Interior, Institute of Geology and Geophysics, Chinese Academy of Sciences, Beijing 100029, China
[2]Department of Resources & Environmental Engineering, Guilin University of Technology, Guilin 541004, China
[3]National Astronomical Observatories, Chinese Academy of Sciences, Beijing, China
[*]Corresponding author. E-mail: linyt@mail.igcas.ac.cn

(Received 22 October 2012; revision accepted 04 July 2013)

Abstract–Grove Mountains (GRV) 020090 is an enriched lherzolitic shergottite, distinct from other lherzolitic shergottites, except RBT 04262/1. Its characteristics include high abundance of plagioclase (24.2 vol% in the nonpoikilitic area), presence of K-feldspar, common occurrence of baddeleyite, high FeO contents of olivine (bimodal peaks at Fa 33 mol% and Fa 41 mol%) and low-Ca pyroxenes (bimodal peaks at Fs 23.8–31.7 mol% and Fs 25.7–33.9 mol%), and significant LREE enrichment of phosphates (500–610 × CI). The bulk composition of GRV 020090 suggests derivation from partial melting of an enriched reservoir. However, the REE patterns of the cores of pigeonite oikocrysts and the olivine chadacrysts are indistinguishable from those of GRV 99027 and other moderately depleted lherzolitic shergottites, and reveal a LREE-depleted pattern of the primordial parent magma. We propose that the primordial parent magma of GRV 020090 was derived from a moderately depleted Martian upper mantle reservoir, and later the residual melt was contaminated by oxidized and enriched Martian crustal materials as it ascended up to the subsurface. GRV 020090 and RBT 04262/1 may have sampled an igneous unit different from other lherzolitic shergottites.

INTRODUCTION

Lherzolitic shergottites are a small and rather homogeneous subgroup of shergottites, with about 10 unpaired finds recorded in the Meteoritical Bulletin Database. The first three meteorites (ALHA77005, Y 793605, LEW 88516) share similar petrography, mineral chemistry, and geochemistry, and were probably ejected from the same igneous unit on Mars (Lundberg et al. 1990; Harvey et al. 1993; Treiman et al. 1994; Ikeda 1997; Warren and Kallemeyn 1997; Wadhwa et al. 1999; Nyquist et al. 2001), although the initial isotopic ratios of Nd and Sr of ALHA77005 are distinct from those of LEW 88516 (Borg et al. 2002). Later discovery of four other lherzolitic shergottites, including GRV 99027 (Lin et al. 2003, 2005), NWA 1950 (Gillet et al. 2005), Yamato 000027/47/97 (Mikouchi and Kurihara 2008), and Yamato 984028 (Hu et al. 2011; Riches et al. 2011), confirms the similarities of this subgroup, despite variations in shock and thermal metamorphism. These lherzolitic shergottites are also referred to as an intermediate subgroup based on their moderate depletion of LREE (Bridges and Warren 2006).

GRV 020090 was found on the blue ice in the Grove Mountains region, Antarctica, by the Chinese Antarctic Expedition in austral summer season of 2002. It was classified as a new lherzolitic shergottite, based on its petrography and mineral chemistry (Miao et al. 2004). However, GRV 020090 also shows obvious differences from other lherzolitic shergottites, e.g., its higher modal abundance of plagioclase (18.1 vol% versus 5.8–9.5 vol%), more FeO enrichments of ferroan mafic silicates and TiO_2 enrichment of chromite. In addition, GRV 020090 shows light rare earth element (LREE)-enriched patterns (Lin et al. 2008b; Jiang and Hsu 2012). In situ Pb-Pb dating of baddeleyite in GRV

© The Meteoritical Society, 2013.

020090 gave an age of 192 ± 10 (2σ) Ma (Jiang and Hsu 2012). Recently, RBT 04262/04261 was reported as a new enriched lherzolitic shergottite, similar to GRV 020090 in petrography, mineral chemistry (Anand et al. 2008; Mikouchi et al. 2008), and LREE-enriched patterns (Usui et al. 2010).

Although GRV 020090 and RBT 04262/1 contain lower olivine abundances (28.9–39.4 vol%) (Miao et al. 2004; Mikouchi et al. 2008; Usui et al. 2010) than the definition of terrestrial lherzolites (≥ 40 vol%), they share most petrographic and mineral chemistry features of typical lherzolitic shergottites. In addition, GRV 99027, a moderately depleted lherzolitic shergottite, is also low in olivine abundance (32.1 vol%) (Lin et al. 2005). Hence, we use the term "lherzolitic" for both GRV 020090 and RBT 04262/1 in this paper. The geochemical enrichments of GRV020090 and RBT 04262/2 have been explained by derivation from oxidized and enriched mantle reservoirs (Shearer et al. 2008; Jiang and Hsu 2012), or sampling the top layer of stratigraphy of the lherzolitic shergottite igneous block (Mikouchi et al. 2008). GRV 020090 and RBT 04261/2 probably represent a new enriched subgroup of lherzolitic shergottites. Another meteorite, NWA 4468, could also be a member of the enriched subgroup of lherzolitic shergottites, although it was reported as an olivine basaltic shergottite (Irving et al. 2007). NWA 2646 and NWA 4797 are olivine-bearing poikilitic shergottites, but their pyroxene oikocrysts have reversed zoning, with high-Ca cores and low-Ca rims (Bunch et al. 2005; Irving et al. 2008), distinct from all other lherzolitic shergottites.

We conducted a comprehensive petrographic and mineral chemical study of GRV 020090, to clarify its petrogenesis and genetic relationship with other lherzolitic shergottites. In particular, we tried to understand whether the LREE enrichment of GRV 020090 was inherent or resulted from later contamination with oxidized and enriched crustal materials. Preliminary results were reported by Lin et al. (2008b).

EXPERIMENTAL

Petrographic observation of two polished sections of GRV 020090 was conducted with an optical microscope and a scanning electron microscope (SEM) of type LEO 1450VP equipped with energy dispersive spectrometry (EDS). Major and minor element compositions of minerals were analyzed with an electron probe microanalyzer (EPMA) of type JEOL 8100 equipped with 4 wavelength-dispersive spectrometers (WDS). The measurements were performed under 15 kV of accelerating voltage with a beam current of 20 nA. A defocused beam (with a diameter of 5 μm) was applied to feldspars to avoid evaporating alkali elements. Diopside (Ca and Si), jadite (Na), almandine garnet (Fe and Al), orthoclase (K), rhodonite (Mn), forsterite (Mg), apatite (P), Tugtupite (Cl), synthetic eskolaite (Cr), and rutile (Ti) were used as standards, and the results were treated with the traditional ZAF method. Peak overlapping of K_α line of V by K_β line of Ti was corrected.

In situ analysis of the rare earth elements (REE) and other trace elements in phosphates was carried out by inductively coupled plasma mass spectrometry with laser-ablation system (LA-ICP-MS). The ICP-MS type Agilent 7500A was optimized with NIST 610 glass. The constituent minerals were ablated by a GeoLas UV-193 nm laser working at a diameter of 40–80 μm and a frequency of 4 Hz. NIST 610 glass was used as the standard, with Ca as the reference element. The integrated counts were subtracted by the backgrounds measured before ablation.

REE and other trace elements in silicate minerals were measured by secondary ion mass spectrometry (SIMS) with the CAMECA ims 1280 at the Institute of Geology and Geophysics, Chinese Academy of Sciences. An O_2^- beam of 3 nA and approximately 20 μm in diameter was used. Instead of the traditional energy filtering method, high mass resolution ($m/\Delta m \geq 9500$) was used in this study, which is high enough to separate peak overlaps of heavy REE (HREE) by mono-oxides of light REE (LREE). A total of 26 ions (including 16 masses of REEs, Y, U, Th, Pb, Zr, Hf, Sc, Ti, Ca, and Si) were counted by peak switching technique. Reproducibility of the peak positions was checked during peak switching at high mass resolution mode, and was better than 10 ppm compared to a width of approximately 20 ppm for the flat peak tops. Cycling of approximately 30 min ensured a stable magnetic field. The wait time was 1–10 s, depending on the mass differences between adjacent peaks. The counting time for LREE was twice as long as that for HREE for analyses of pyroxenes and olivine, with a total measurement time of 80–120 min, depending on the REE concentrations of the samples. The same conditions were also applied to plagioclase. The measurements were corrected for the dead time and background of the electron multiplier (EM). The results were calibrated with NIST 610 glass, using Si as the reference element.

RESULTS

Petrography

GRV 020090 weighs 7.5 g and appears very fresh with a glassy black fusion crust that shows flowing lines

from the top of the cone (Fig. 1). The meteorite is composed of two textural lithologies (Fig. 2), i.e., the poikilitic (43.6 vol%) and nonpoikilitic (56.4 vol%), typical of lherzolitic shergottites. The poikilitic lithology consists of several pyroxene oikocrysts (up to 6.9 mm in length) with olivine chadacrysts and small inclusions of chromite. The pyroxene oikocrysts are concentrically zoned, with pigeonite cores mantled by augite (Fig. 2b). The modal composition of the poikilitic lithology was determined from the surface areas of individual minerals, and consists of (normalized to 100 vol%) 15.5 vol% olivine, 50.9 vol% pigeonite, 31.6 vol% augite, and 1.9 vol% chromite with a few melt inclusions in olivine and pyroxene. The nonpoikilitic region is composed of euhedral grains of olivine (39.9 vol%) and pyroxenes (32.1 vol%) and interstitial laths of plagioclase (24.2 vol%), with minor phosphates (1.5 vol%), chromite (1.7 vol%), sulfide (0.2 vol%), and trace ilmenite and baddeleyite. The modal compositions of the individual textural lithologies and the whole meteorite are given in Table 1, and are compared with GRV 99027 and RBT 04262.

Plagioclase has smooth surfaces compared with the heavily fractured olivine, pyroxenes, and phosphates (Figs. 3a and 3b), and has been converted to maskelynite. No schlieren or other melting textures were observed in the maskelynite, although a sharp and very thin shock-induced melt vein cut through maskelynite and chromite (Fig. 3a). Compositional heterogeneity of maskelynite is evident in BSE images, with darker (albite-rich) rims (Figs. 3a and 3b). Furthermore,

Fig. 1. GRV 020090 with glassy black fusion crust; note the flow lines from the top of the cone. The bond grids are 1 cm × 1 cm.

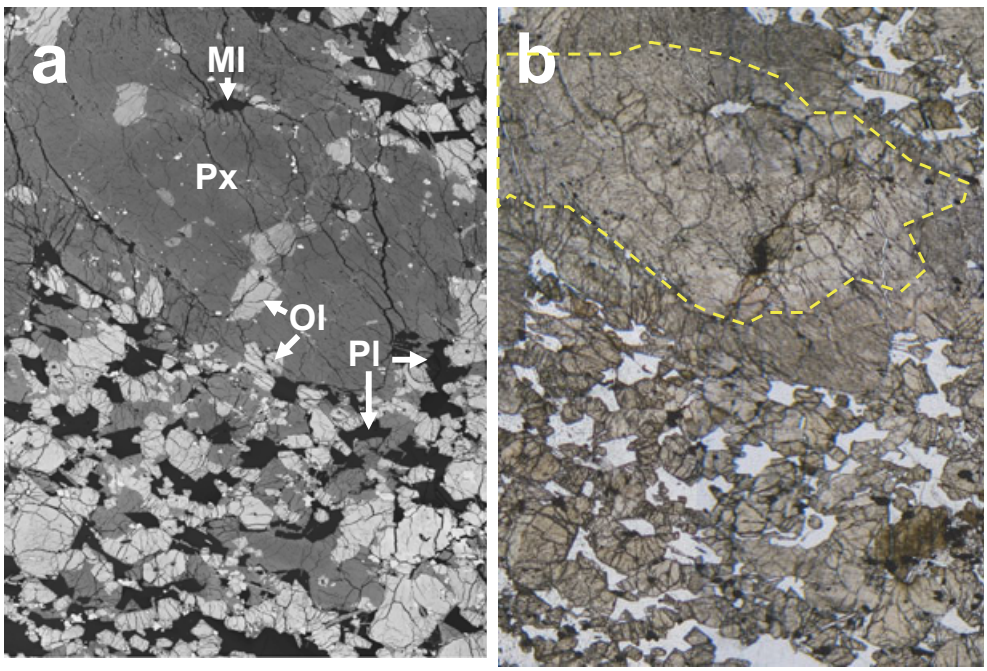

Fig. 2. Microphotographs of GRV 020090. (a) Backscattered electron (BSE) image and (b) transmitted light. The upper parts of the images show the poikilitic lithology, consisting mainly of a concentrically zoned pyroxene oikocryst (Px) with a few olivine (Ol) chadacrysts and small grains of chromite (white in BSE image and black under transmitted light). Note a large melt inclusion (MI) in the pyroxene oikocryst. The dashed line in the right image indicates the boundary between the pigeonite core and the augite mantle. The lower parts of the images show the nonpoikilitic lithology, consisting of euhedral olivine and pyroxene with interstitial plagioclase (Pl, dark in the left and white in the left). The width of the field of view is 6 mm.

Table 1. Modal compositions of GRV 020090 and other lherzolitic shergottites (normalized to 100 vol%).

	GRV 020090				GRV 99027	RBT 04262		Others[a]
	Poikilitic (43.6%)	Interstitial (56.4%)	Bulk		Bulk	Bulk		Bulk
Olivine	15.5	39.9	29.3	28.9	32.1	30.0	39.4	40–59.7
Pigeonite	50.9	32.1	40.3	35.6	55.3	43.0	28.0	9.2–33
Augite	31.6	#	13.8	15.7	5.0	10.0	12.4	3.6–17
Chromite	1.9	1.9	1.9	1.7	1.1	2.0	1.5	0.6–1.5
Ilmenite		+	+	+	+	+	0.2	<0.3
Maskelynite		24.2	13.6	18.1	5.8	13.0	15.9	8–11.5
Merrillite[b]		1.5	0.9		0.5	1.0	1.1	0.4–0.9
Sulfide		0.3	0.2		0.2	+	0.3	<0.2
Melt	+	+	+	+	+	+	1.1	+
References	This work	This work	This work	1	2	3	4	5–7

[a]ALHA77005, Y793605, and LEW 88516.
[b]Including apatite.
+ = minor; # = included in pigeonite.
Literature: 1—Miao et al. (2004); 2—Lin et al. (2005); 3—Mikouchi et al. (2008); 4—Usui et al. (2010); 5—Treiman et al. (1994); 6—Ikeda (1997); 7—Mikouchi and Miyamoto (1997).

K-feldspar was locally found as the outmost rims of plagioclase (Fig. 3b). This is the first occurrence of K-feldspar in lherzolitic shergottites, except for a few grains in melt inclusions. Very fine-grained mixtures of Cr-rich (probably chromite) and Si-rich (probably silica) materials often coexist with K-feldspar.

Chromite was encountered as a common minor phase in both textural lithologies, but has distinct occurrences. In the poikilitic area, it occurs as single small diamond-shaped inclusions (<50 μm) in olivine chadacrysts and pyroxene oikocrysts. In contrast, in the nonpoikilitic lithology, chromite coexists with ilmenite as chromite-ilmenite assemblages interstitial to silicates (Fig. 3c). More than 20 grains (up to 5 × 10 μm) of baddeleyite were encountered, all coexisting with ilmenite (Fig. 3c). Pentlandite is usually associated with the chromite-ilmenite assemblages, and many of the grains contain vein-like magnetite (Fig. 3d). Phosphates are merrillite and apatite, with the former more abundant than the latter (Figs. 3a and 3b). Apatite always intergrows with merrillite, and the merrillite-apatite intergrowth occurs as laths in plagioclase or at boundaries between plagioclase and mafic silicates.

Melt inclusions are common in olivine and, to a lesser extent, in pyroxene in both textural lithologies, with round or elongated shapes (Figs. 3e and 3f). Pyroxene crystals are typically found on the walls of the inclusions, with a few euhedral inclusions in the mesostasis of the center. Two kinds of mesostasis, i.e., Na-rich and K-rich, were encountered. Silica occurs in some melt inclusions, and usually coexists with K-rich mesostasis. Tiny grains of chromite and needles of phosphate are enclosed in the mesostasis.

Mineral Chemistry

Olivine

Olivine shows bimodal compositions (Fig. 4). The chadacrysts (Fa 29.7–40.1 mol%, with a peak at Fa 33 mol%) contain lower FeO contents than those in the nonpoikilitic area (Fa 35–43.7 mol%, with a peak at Fa 41 mol%). In addition, the Fa contents of olivine chadacrysts appear to increase from Fa 32.8–33.5 mol% at the center of the pyroxene oikocrysts to Fa 36.4–37.3 mol% at the margin. Regardless of the variation among the grains, individual olivine chadacrysts are rather homogeneous in composition. In contrast, the FeO contents of olivine in the nonpoikilitic area slightly increase toward the rims, with CaO content decreasing from 0.35 wt% at the cores to 0.10 wt% at the rims. Another minor component is MnO (0.43–0.84 wt%), with a mean FeO/MnO ratio of 48.5 ± 5.2 (1σ). The analysis averages and ranges are given in Table 2.

Pigeonite and Augite

Pigeonite also shows a bimodal compositional distribution (Fig. 5), with lower FeO contents of the oikocrysts (Fs 23.8–31.7 mol%) than those of the interstitial grains (Fs 25.7–33.9 mol%). The concentrations of the minor elements of Al_2O_3, TiO_2, and Cr_2O_3 differ, depending on the pyroxene occurrence (Figs. 6a and 6b). The interstitial pigeonite grains show a positive relationship between the contents of Al_2O_3 (0.36–1.31 wt%) and Cr_2O_3 (0.08–0.52 wt%), with 0.16–0.87 wt% TiO_2. In contrast, the pigeonite oikocrysts show a positive correlation between the contents of Al_2O_3 (0.4–0.78 wt%) and TiO_2 (<0.66 wt%), with 0.29–0.89 wt% Cr_2O_3, except for a few analyses of the rims of

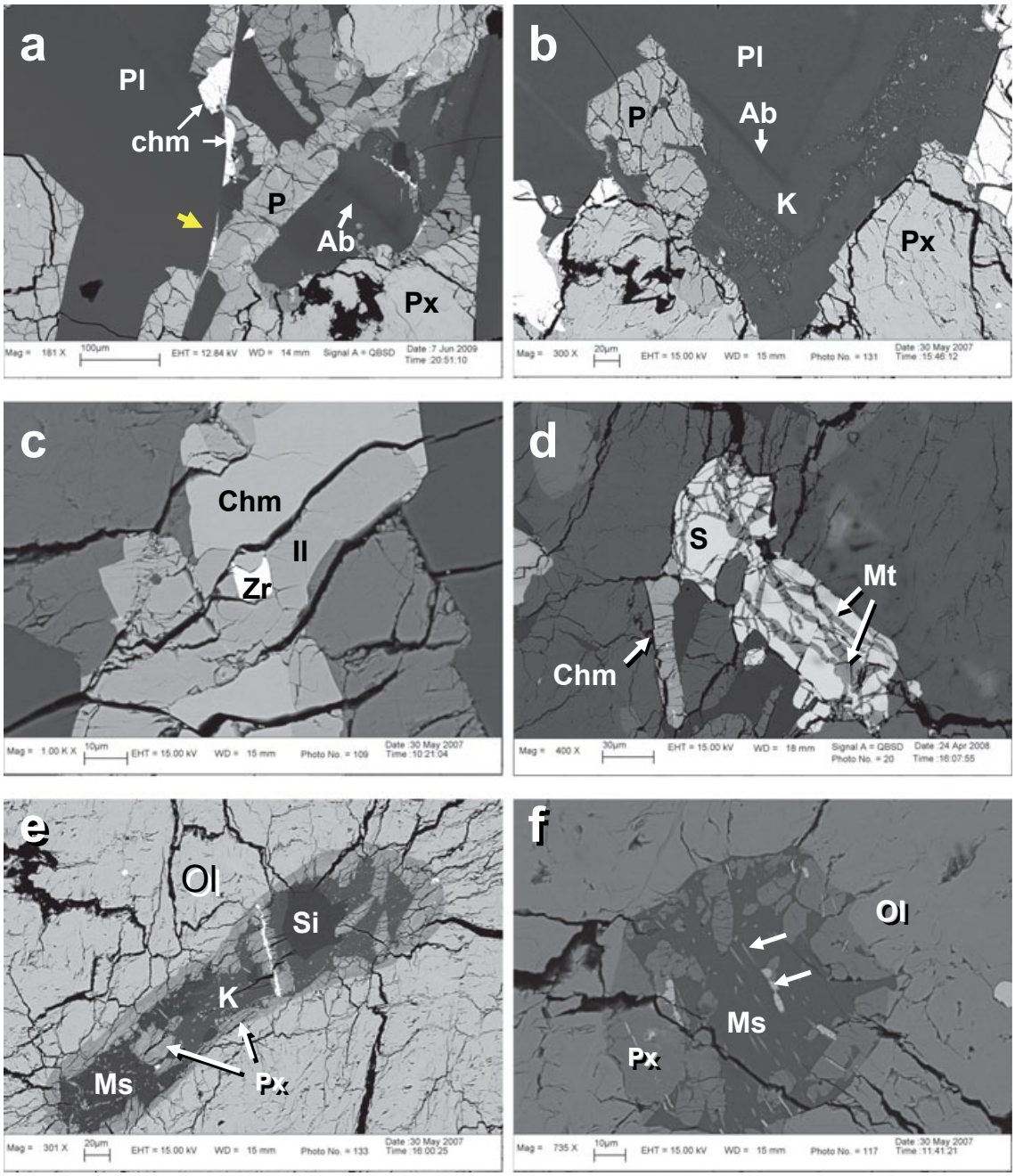

Fig. 3. Backscattered electron (BSE) images of GRV 020090. (a) Plagioclase with a smooth surface, compared with fractured mafic silicates. Note the darker albite-rich plagioclase (Ab) layers on the right. A tiny melt vein (arrow) cuts through plagioclase and chromite (Chm). Phosphates (P) are intergrowths of merrillite (darker) and apatite (brighter). (b) Zoning texture of feldspars, from Ca-rich (Pl) at the core to Na-rich (Ab), and then to K-rich (K) at the rim. The layer within the K-feldspar is a very fine-grained mixture of Cr-rich (probably chromite) and Si-rich (probably silica) materials. (c) An euhedral grain of baddeleyite (Zr) enclosed in ilmenite (Il) in the chromite-ilmenite assemblage. (d) Assemblage of pentlandite (S) and vein-like magnetite (Mt). (e) An elongated melt inclusion with pyroxenes (Px) in olivine. The center of the melt inclusion contains euhedral pyroxene grains and Na-rich (Ms) and K-rich (K) mesostasis. A large silica (Si) grain occurs in the K-rich mesostasis. (f) Another melt inclusion in olivine, consisting of pyroxenes (Px), Na-rich mesostasis (Ms), and needle-like phosphates (arrows).

the pigeonite oikocrysts, which plot within the ranges of the interstitial grains. The FeO/MnO ratio of pigeonite is 28.7 ± 3.1. Augite mainly occurs as rims on the pigeonite oikocrysts. It has compositions of $Fs_{14.8–22.0}En_{43.9–54.3}Wo_{23.7–39.8}$, with minor TiO_2 (0.1–0.8 wt%), Cr_2O_3 (0.5–0.9 wt%), Al_2O_3 (1.0–2.1 wt%),

Table 2. Average compositions of olivine and pyroxenes in GRV 020090 (wt%).

	Olivine		Augite	Pigeonite	
	Poikilitic	Nonpoikilitic	Poikilitic	Poikilitic	Nonpoikilitic
SiO_2	37.1 ± 0.6	36.4 ± 0.5	52.3 ± 0.5	53.8 ± 0.7	53.0 ± 0.8
	35.8–38.1	*35.0–37.4*	*51.6–53.7*	*52.0–55.3*	*51.3–54.3*
TiO_2			0.30 ± 0.11	0.14 ± 0.08	0.37 ± 0.16
			0.19–0.62	*0.04–0.47*	*0.16–0.87*
Al_2O_3			1.43 ± 0.31	0.58 ± 0.16	0.77 ± 0.25
			1.01–2.09	*0.40–1.21*	*0.36–1.32*
Cr_2O_3	0.03 ± 0.04	0.04 ± 0.05	0.74 ± 0.09	0.46 ± 0.14	0.30 ± 0.13
	<0.15	*<0.41*	*0.58–0.93*	*0.24–0.89*	*0.08–0.52*
FeO	29.8 ± 2.4	33.6 ± 1.5	11.1 ± 1.0	16.4 ± 0.8	18.9 ± 1.5
	26.2–34.8	*30.6–37.3*	*9.8–13.6*	*15.1–18.8*	*16.0–23.5*
MnO	0.62 ± 0.08	0.72 ± 0.05	0.45 ± 0.05	0.57 ± 0.07	0.69 ± 0.06
	0.43–0.77	*0.62–0.84*	*0.36–0.53*	*0.43–0.72*	*0.57–0.81*
MgO	32.7 ± 1.8	29.5 ± 1.2	16.8 ± 0.8	23.9 ± 1.4	20.5 ± 0.7
	28.7–35.4	*27.6–32.5*	*15.6–18.9*	*19.8–26.1*	*18.8–22.7*
CaO	0.15 ± 0.05	0.18 ± 0.06	15.5 ± 1.4	3.43 ± 1.18	5.08 ± 1.32
	0.07–0.29	*0.07–0.34*	*11.5–17.8*	*1.96–6.91*	*2.45–7.76*
Na_2O			0.21 ± 0.04	0.07 ± 0.03	0.10 ± 0.04
			0.11–0.29	*<0.19*	*<0.20*
Fa/Fs	33.9 ± 3.0	39.1 ± 1.9	18.2 ± 1.6	25.9 ± 1.3	30.4 ± 2.2
	29.7–40.1	*35.0–42.9*	*16.2–22.0*	*24.1–30.3*	*25.7–37.4*
Wo			32.6 ± 3.1	7.0 ± 2.4	10.5 ± 2.8
			23.7–37.7	*3.9–14.1*	*5.0–16.4*
En			49.2 ± 2.0	67.1 ± 3.4	59.0 ± 1.8
			46.1–54.3	*57.6–71.9*	*53.9–65.1*

Italic numbers are the ranges; the totals of individual analyses are between 98 and 102 wt%.

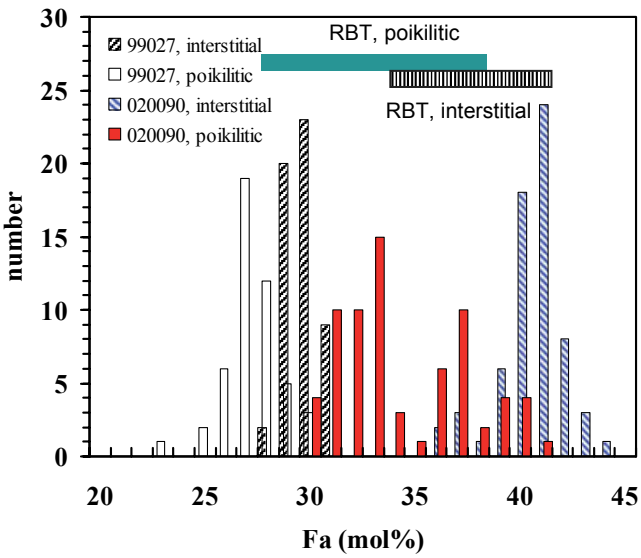

Fig. 4. Histogram of the Fa contents of olivine from GRV 020090, showing a bimodal distribution. The olivine chadacrysts have lower Fa contents than the interstitial grains. Literature data for the lherzolitic shergottite GRV 99027 are from Lin et al. (2005) and the ranges of RBT 04262 (RBT, dashed lines for nonpoikilitic lithology, and solid lines for poikilitic) are from Mikouchi et al. (2008).

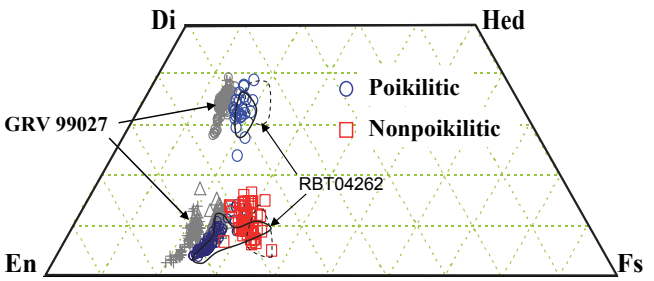

Fig. 5. Quadrilateral diagram of pyroxenes from GRV 020090. Pigeonite also shows a bimodal distribution, and the oikocrysts are FeO-poor compared with the interstitial grains. Literature data for the lherzolitic shergottite GRV 99027 are from Lin et al. (2005), and for RBT 04262 are from Usui et al. (2010).

MnO (0.3–0.5 wt%), and Na_2O (0.1–0.4 wt%). The analysis averages and ranges are listed in Table 2.

Feldspars

Both K_2O-rich feldspar and K_2O-poor plagioclase were found. From the cores to the rims, compositions of feldspars vary from labradorite to oligoclase, and to orthoclase-rich (Table 3; Fig. 7). Plagioclase

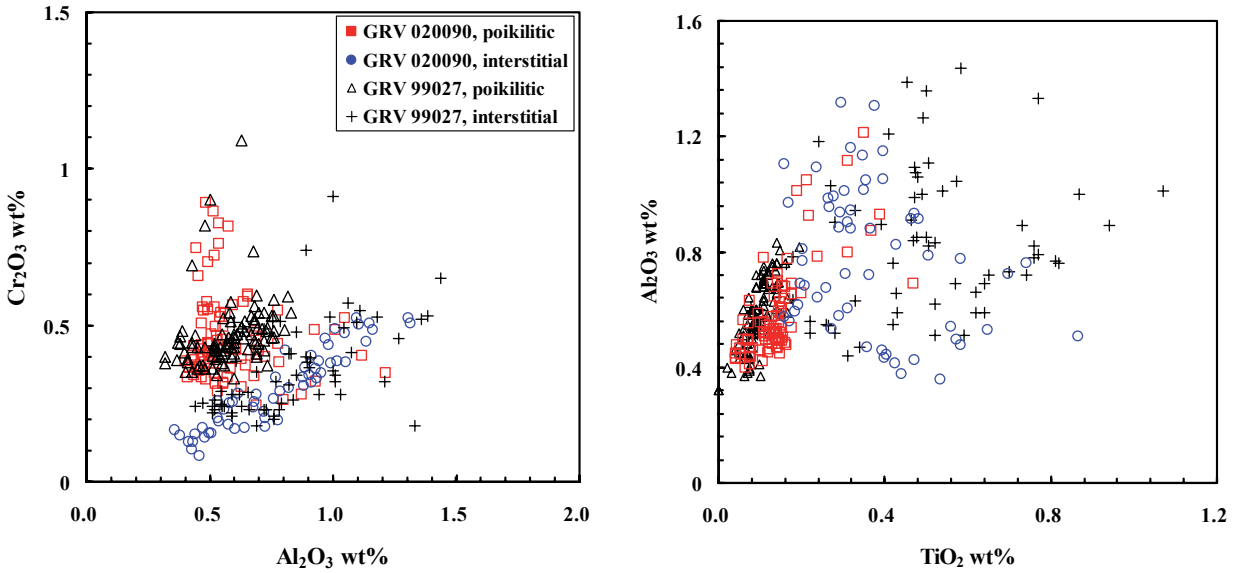

Fig. 6. Compositions of pigeonite from GRV 020090. (a) Al_2O_3 versus Cr_2O_3, showing a positive correlation for the interstitial grains; (b) TiO_2 versus Al_2O_3, showing a narrow and positive correlation for the pigeonite oikocrysts. A few analyses of the pigeonite oikocrysts plot within the ranges of the interstitial grains, and are located at the margins of the latter. Literature data are from Lin et al. (2005).

Table 3. Average and representative compositions of plagioclase and K-feldspar in GRV 020090 (wt%).

			Pl				Pl	K-feld	Pl	K-feld
	Pl	K-feld	1[a]	1	2[a]	2	3		4	
SiO_2	56.4 ± 1.9	65.4 ± 0.6	59.7	55.2	59.3	54.5	59.9	67.0	62.2	65.0
	52.9–61.9	*63.6–66.5*								
TiO_2	0.07 ± 0.04	0.20 ± 0.03	0.06	0.08	0.09	0.10	0.10	0.12	0.13	0.12
	<0.18	*0.13–0.26*								
Al_2O_3	26.9 ± 0.9	18.9 ± 0.6	24.6	27.6	25.0	28.0	25.4	19.1	24.2	19.7
	24.6–28.5	*18.2–21.3*								
Cr_2O_3	0.01 ± 0.02	0.02 ± 0.02	0.03	0.04	b.d.	b.d.	b.d.	b.d.	b.d.	b.d.
	<0.08	*<0.08*								
FeO	0.45 ± 0.11	0.29 ± 0.12	0.28	0.61	0.43	0.50	0.31	0.14	0.33	0.27
	0.25–0.86	*0.12–0.60*								
MgO	0.08 ± 0.02	0.01 ± 0.01	0.05	0.12	0.05	0.08	0.03	0.02	0.04	0.02
	0.04–0.15	*<0.05*								
CaO	9.85 ± 1.22	0.92 ± 0.52	7.52	11.6	7.82	11.6	8.39	0.82	6.11	1.32
	7.16–12.0	*0.26–2.87*								
Na_2O	5.33 ± 0.72	4.80 ± 0.58	7.21	5.43	6.81	5.27	6.69	5.13	7.29	5.36
	4.41–7.12	*3.88–6.42*								
K_2O	0.43 ± 0.16	8.50 ± 1.18	0.60	0.39	0.74	0.39	0.59	8.77	1.11	7.56
	0.18–0.81	*5.20–10.5*								
Total			100.1	101.0	100.3	100.4	101.4	101.2	101.4	99.3
An	47.7 ± 6.2	4.5 ± 2.5	36.1	55.9	37.4	56.3	39.7	3.9	28.8	6.4
	33.6–57.2	*1.3–13.8*								
Ab	46.7 ± 5.9	42.3 ± 4.9	62.5	47.3	59.0	46.2	57.3	44.3	62.1	47.0
	38.8–61.2	*34.1–56.1*								
Or	2.5 ± 0.9	49.4 ± 7.0	3.4	2.3	4.2	2.2	3.3	49.8	6.2	43.7
	1.0–4.7	*30.2–60.4*								

[a]Relatively dark zones of plagioclase.
Pl = plagioclase; K-feld = K-feldspar; b.d. = below detection limit. Italic numbers are the ranges.

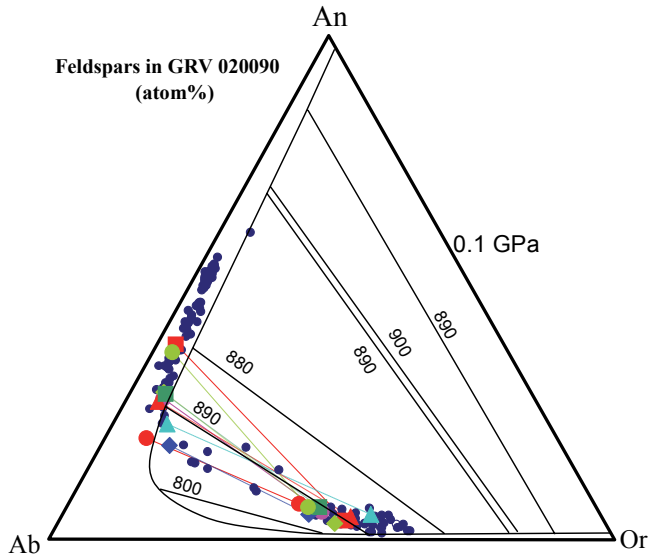

Fig. 7. Compositions of coexisting K-rich feldspar and plagioclase in GRV 020090, plotting on the phase boundary at 0.1 GPa and approximately 890 °C. The paired K-rich feldspar and plagioclase analyses are labeled with similar symbols and linked by lines. The phase diagram is from Presnall (1995).

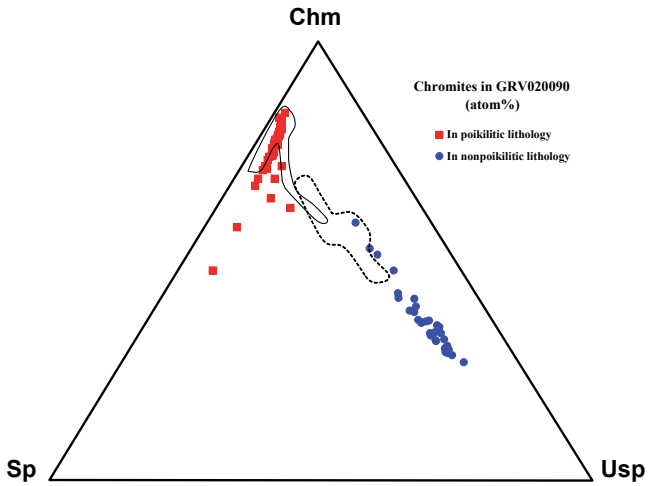

Fig. 8. Chromites from the different lithologies in GRV 020090 show distinct compositional variations. The grains enclosed in olivine and pyroxene in the poikilitic lithology are ulvö-spinel (Usp)—poor with a wide range of spinel (Sp)/chromite (Chm) ratios, whereas those in the nonpoikilitic lithology are highly Usp-enriched, with low and nearly constant spinel contents. The fields for chromites in the poikilitic (solid line) and in the nonpoikilitic (dashed line) lithologies of GRV 99027 are from Lin et al. (2005).

contains minor K_2O (0.18–1.46 wt%), negatively correlated with An contents. Minor components are FeO (0.21–0.86 wt%) and MgO (<0.15 wt%). K-feldspar has a compositional range of $An_{1.4–6.9}Ab_{35.5–51.1}Or_{62.8–42.8}$ with lower FeO (0.28 ± 0.12 wt%). Average and representative compositions of plagioclase and K-feldspar are given in Table 3.

Chromite and Ilmenite

Chromite is a solid solution of spinel (Sp), chromite (Chm), magnetite (Mt), and ulvö-spinel (Usp), and its composition is related to its occurrence (Fig. 8). The small and euhedral chromite inclusions in the olivine chadacrysts and pigeonite oikocrysts are typically poor in Usp (2.33–8.63 mol%) and Mt (5.4–10.6 mol%), varying, with a relatively constant Sp/Usp ratio (4.3 ± 0.5), from $Chm_{78.9}Sp_{11.8}Mt_{6.5}Usp_{2.3}$ to $Chm_{44.6}Sp_{40}Mt_{8.6}Usp_{6.6}$. In comparison, those grains interstitial to silicates are usually larger and anhedral, and commonly coexist with ilmenite. They are richer in Usp (4.61–50.4 mol%) and Mt (10.7–25.2 mol%), varying, with a relatively constant Sp/Chm ratio (0.29 ± 0.04), from $Chm_{51.2}Sp_{10.5}Mt_{14.5}Usp_{23.8}$ to $Chm_{22.1}Sp_{6.6}Mt_{21}Usp_{50.4}$ (Fig. 8). In addition, chromites in the poikilitic lithology contain more MgO (3.34–5.81 wt%) and less MnO (0.17–0.62 wt%) than those in the nonpoikilitic lithology (2.17–3.35 wt% MgO, 0.44–0.72 wt% MnO). Chromite in contact with ilmenite shows a decreasing trend of TiO_2 contents from 19.1 wt% at the core to 17.3 wt% at the rim. Compositions of ilmenite are rather homogeneous, containing 42.2–44.1 wt% FeO and 51.3–53.3 wt% TiO_2 with minor Cr_2O_3 (0.47–2.44 wt%), MgO (3.37–4.43 wt%), and MnO (0.55–0.81 wt%). Average and representative analyses of chromite and ilmenite are given in Table 4.

Phosphates

Merrillite is the most abundant phosphate, and apatite usually intergrows with the former at the rims. Besides CaO (45.44–50.39) and P_2O_5 (44.03–47.72 wt%), merrillite contains Na_2O (1.53–2.21), MgO (2–3.59), and FeO (0.68–1.38). Apatite is nearly pure $Ca_5[PO_4]_3(Cl,F,OH)$ with minor FeO (0.37–0.64), MgO (0.08–0.22), and Na_2O (0.35–0.52). No F peak was observed with EDS. The analytical totals of apatite are close to 100% (97.3–99.3 wt%), suggestive of low OH contents, consistent with 0.09–0.6 wt% H_2O determined by secondary ion mass spectrometry (Hu et al. 2012). Representative analyses of apatite and merrillite are given in Table 5.

REE Abundances of Minerals

In situ REE analyses of phosphates (intergrowth of apatite and merrillite), pigeonite, augite, plagioclase,

Table 4. Average compositions of chromite and ilmenite in GRV 020090 (wt%).

	Chm poikilitic	Chm Nonpoikilitic	Il
SiO_2	0.06 ± 0.05	0.01 ± 0.01	0.03 ± 0.03
	<0.32	*<0.05*	*<0.10*
TiO_2	1.58 ± 0.44	15.8 ± 1.7	52.5 ± 0.6
	0.71–3.38	*11.1–19.1*	*51.3–53.3*
Al_2O_3	8.52 ± 2.19	4.13 ± 0.56	0.04 ± 0.05
	5.66–21.0	*3.18–5.35*	*<0.20*
Cr_2O_3	51.9 ± 3.7	21.3 ± 4.5	0.8 ± 0.5
	34.9–56.6	*15.5–34.2*	*0.5–2.4*
FeO	31.7 ± 1.7	55.7 ± 3.2	43.1 ± 0.5
	29.5–36.9	*47.2–60.4*	*42.2–44.1*
MnO	0.44 ± 0.10	0.61 ± 0.06	0.73 ± 0.07
	0.17–0.62	*0.48–0.72*	*0.55–0.81*
MgO	5.02 ± 0.56	2.56 ± 0.24	3.69 ± 0.27
	3.00–5.81	*2.17–3.34*	*3.37–4.43*
Fe^{3+}/Fe^{a}	0.16 ± 0.01	0.23 ± 0.02	
	0.12–0.20	*0.18–0.28*	
Chm[a]	70.9 ± 5.6	29.9 ± 6.2	
	44.6–78.9	*22.1–47.4*	
Sp	17.3 ± 4.2	8.6 ± 1.1	
	11.8–40.0	*6.6–11.1*	
Mt	7.5 ± 0.9	19.4 ± 2.7	
	5.4–10.6	*12.3–25.2*	
Usp	4.1 ± 1.1	42.1 ± 4.7	
	1.9–8.6	*29.4–50.3*	

[a]Fe^{3+} and the components were calculated based on the stoichiometric formula of $M^{2+}N_2^{3+}O_4$.
Italic numbers are the ranges; b.d. = below detection limit.

and olivine are summarized in Table 6. Phosphates contain high REE (520–610 × CI), and are LREE-enriched (La/Lu: 1.33–1.49 × CI) with significant negative Eu anomalies (Eu/Eu: 0.67–0.77 × CI) (Fig. 9a). CI-normalized concentrations of HREE of phosphates decrease from Tb (645–756 × CI) to Lu (420–500 × CI). The REE concentrations of pigeonite are related to their occurrences, and are lower in the poikilitic lithology than in the nonpoikilitic lithology (Fig. 9c; Table 6). In addition, the core of the pigeonite oikocryst contains the lowest REE concentrations (SIMS-1 in Table 6) of any of the pyroxenes. The augite mantle of the pigeonite oikocryst shows an increasing trend of REE concentrations toward the rim (SIMS-4 and -5 in Table 6). Both pigeonite and augite are HREE-enriched (Lu/La 11.0–13.5 × CI for augite, 21–110 × CI for pigeonite) with small negative Eu anomalies except for a few analyses (Figs. 9c and 9d). Plagioclase shows typical LREE-rich patterns with large positive Eu anomalies (10–17 × CI, Fig. 9b). Olivine is LREE-depleted (La 10^{-3} × CI, Lu 0.8 × CI, Fig. 9b).

DISCUSSION

Genetic Link with Other Lherzolitic Shergottites

Distinction between GRV 020090 and Other Depleted or Intermediate Lherzolitic Shergottites

A remarkable feature of most lherzolitic shergottites is their similarity. Most lherzolitic shergottites (including Y-793605, ALHA77005, LEW 88516, GRV 99027, Y-984028, NWA 1950, Y-000027/47/97) share similar bulk compositions, petrographies, and mineral chemistries (e.g., Lundberg et al. 1990; Harvey et al. 1993; Ebihara et al. 1997; Ikeda 1997; Mikouchi and Miyamoto 1997; Warren and Kallemeyn 1997; Wadhwa et al. 1999; Gillet et al. 2005; Lin et al. 2005; Mikouchi and Kurihara 2008; Hu et al. 2011). In addition, they have ages close to approximately 180 Ma (Nyquist et al. 2001; Borg et al. 2002; Liu et al. 2011). It is possible that most lherzolitic shergottites came from the same igneous unit on Mars. This scenario is consistent with their undistinguishable ejection ages (Eugster et al. 2002; Gillet et al. 2005; Kong et al. 2007).

GRV 020090 shares the typical petrography and mineral chemistry of lherzolitic shergottites, such as an assemblage of poikilitic and nonpoikilitic lithologies and the bimodal compositions of olivine, pyroxenes, and chromite. We confirm the classification of GRV 020090 as a lherzolitic shergottite despite its lower abundance of olivine (29.3 vol%) relative to the definition of terrestrial lherzolite (40–90 vol% olivine). Low abundances of olivine were also reported in GRV 99027 and RBT 04262 (Table 1). On the other hand, differences between GRV 020090 and other lherzolitic shergottites are also obvious. Because of the similarity of GRV 99027 to most lherzolitic shergottites (Lin et al. 2005, 2008a), hereafter we compare GRV 020090 mainly with GRV 99027. As noted above, GRV 020090 contains a significantly higher abundance of plagioclase (13.6 vol% in the whole rock and 18.1 vol% in the interstitial part) than GRV 99027 (5.8 vol% and 14.6 vol%, respectively) (Lin et al. 2005). Furthermore, K-feldspar was encountered only in GRV 020090, as the outermost rims of plagioclase. Consistent with the presence of K-feldspar, plagioclase contains higher K_2O in GRV 020090 than in GRV 99027 (Fig. 7). This suggests that the parent magma of GRV 020090 could be relatively K-enriched. GRV 020090 is also distinguished from GRV 99027 and other lherzolitic shergottites by its more ferroan mafic mineral compositions (Figs. 4–5). The Fa-contents of the olivine chadacrysts in GRV 020090 are even higher than those of the interstitial grains in GRV 99027. Furthermore, the pigeonite oikocrysts in GRV 020090 contain as high FeO as those grains in the nonpoikilitic lithology of

Table 5. Representative compositions of phosphates in GRV 020090 (wt%).

	Apatite				Merrillite			
SiO_2	b.d.	b.d.	b.d.	b.d.	b.d.	b.d.	0.16	0.15
TiO_2	0.10	0.12	0.05	0.07	0.05	b.d.	0.01	0.00
FeO	0.64	0.40	0.45	0.38	1.08	1.20	1.13	0.84
MnO	0.07	0.11	0.11	0.05	0.10	0.10	0.04	0.04
MgO	0.22	0.12	0.13	0.20	3.18	3.01	3.32	3.47
CaO	52.5	52.5	52.2	52.5	47.4	46.6	47.8	48.2
Na_2O	0.46	0.52	0.42	0.43	2.06	2.21	1.91	2.13
K_2O	b.d.	0.05	0.04	0.04	0.05	0.06	0.08	0.05
P_2O_5	41.2	41.6	40.5	41.7	47.0	46.0	45.9	46.5
Cl	4.99	5.08	5.43	5.01	b.d.	b.d.	b.d.	b.d.
Total	99.12	99.32	98.15	99.28	101.03	99.23	100.32	101.47
Cations per formular unit								
Si	0.000	0.000	0.000	0.000	0.000	0.000	0.029	0.026
Ti	0.007	0.008	0.003	0.005	0.007	0.002	0.001	0.000
Fe	0.046	0.028	0.033	0.027	0.160	0.182	0.170	0.124
Mn	0.005	0.008	0.008	0.004	0.016	0.015	0.006	0.006
Mg	0.028	0.015	0.017	0.025	0.839	0.811	0.886	0.915
Ca	4.796	4.776	4.851	4.768	8.996	9.025	9.166	9.131
Na	0.076	0.085	0.071	0.070	0.708	0.774	0.664	0.729
K	0.001	0.005	0.004	0.004	0.012	0.014	0.017	0.012
P	2.974	2.991	2.979	2.996	7.047	7.029	6.948	6.961
Cl	0.720	0.732	0.799	0.720	0.002	0.006	0.000	0.000
Sum	8.652	8.648	8.765	8.619	17.79	17.86	17.89	17.90

b.d. = below detection limit.

GRV 99027. It is, thus, evident that GRV 020090 is not paired with GRV 99027.

A remarkable feature of GRV 020090 is the very high concentration of REEs of phosphates with negative Eu-anomalies and LREE-enriched patterns (Fig. 9a). The CI-normalized La/Lu ratios of 1.33–1.49 are even higher than the range of the moderately depleted shergottites (0.8–1.2) (Bridges and Warren 2006). The bulk REE concentrations of GRV 020090 are dominated by phosphates and cannot be produced by fractional crystallization from a magma similar to that which produced the moderately depleted GRV 99027. We therefore classified GRV 020090 as an enriched lherzolitic shergottite.

Possible Paired Ejection with RBT 04262/1

RBT 04262/1 is also an enriched lherzolitic shergottite (Usui et al. 2010). The similarities between both meteorites are evident, with olivine-poor and plagioclase-rich modal compositions, more ferroan mafic silicates, and LREE enrichment of phosphates. In fact, the differences in the modal compositions between GRV 020090 and RBT 04262 are less than the sampling bias of the latter as indicated by the heterogeneity between the paired samples RBT 04262 and 04261 (Usui et al. 2010).

As shown in Fig. 4, the Fa content ranges of olivine in the poikilitic and nonpoikilitic lithologies of GRV 020090 overlap with those of RBT 04262, and both are significantly higher than other lherzolitic shergottites. The compositions of pyroxenes in both meteorites are also almost identical (Fig. 5). Furthermore, the ranges of REEs in pigeonite, augite, olivine, and plagioclase from GRV 020090 (Fig. 9) overlap with those of RBT 04262/1 (Usui et al. 2010), except for the significant Eu depletion of phosphates.

The baddeleyite U-Pb age of GRV020090 was reported to be 196 ± 12 Ma (2σ) (Jiang and Hsu 2012), slightly older than the Rb-Sr internal isochron age of 167 ± 6 Ma (2σ) and the Sm-Nd internal isochron age of 174 ± 14 of RBT 04262 (Shih et al. 2009). However, a similar U-Pb age of approximately 200 Ma for baddeleyite was reported in RBT 04261 (Niihara 2011). The available data are consistent with a paired ejection of GRV 020090 and RBT 04262. However, more analyses, especially cosmic-ray exposure histories, would be required to confirm a genetic relationship.

Two Stages of Crystallization

Based on the observed textures, formation of GRV 020090 can be divided into two episodes, i.e., accumulation of the poikilitic lithology and subsequent crystallization of the nonpoikilitic. Ti-poor chromite was the first mineral precipitated from the original

Table 6. REEs compositions of minerals in GRV 020090 (μg/g).

	Pigeonite (poikilitic)		Augite		Pigeonite (interstitial)				
	Core			Rim				Rim-small	Core-small
	SIMS-1	SIMS-2	SIMS-4	SIMS-5	SIMS-9	SIMS-15	SIMS-16	SIMS-18	SIMS-19
Y	0.858 ± 0.032	1.11 ± 0.03	8.12 ± 0.08	11.8 ± 0.1	17.3 ± 0.2	5.63 ± 0.09	5.33 ± 0.09	9.49 ± 0.3	2.11 ± 0.09
La	0.0018 ± 0.0008	0.0079 ± 0.0026	0.082 ± 0.005	0.145 ± 0.006	0.141 ± 0.007	0.014 ± 0.004	0.048 ± 0.004	0.044 ± 0.01	0.01 ± 0.003
Ce	0.008 ± 0.0027	0.0208 ± 0.0042	0.374 ± 0.015	0.607 ± 0.024	0.629 ± 0.024	0.037 ± 0.008	0.246 ± 0.018	0.309 ± 0.044	0.044 ± 0.011
Pr	0.0014 ± 0.0008	0.002 ± 0.0011	0.102 ± 0.007	0.15 ± 0.006	0.186 ± 0.008	0.013 ± 0.003	0.065 ± 0.005	0.061 ± 0.011	0.009 ± 0.002
Nd	0.0117 ± 0.008	0.0393 ± 0.0105	0.688 ± 0.064	1.18 ± 0.07	1.21 ± 0.08	0.088 ± 0.029	0.427 ± 0.044	0.547 ± 0.115	0.091 ± 0.027
Sm	0.0118 ± 0.0047	0.0315 ± 0.0081	0.435 ± 0.028	0.742 ± 0.042	0.87 ± 0.043	0.078 ± 0.02	0.284 ± 0.019	0.28 ± 0.061	0.071 ± 0.019
Eu	0.0099 ± 0.0028	0.0098 ± 0.0026	0.176 ± 0.01	0.237 ± 0.01	0.272 ± 0.012	0.04 ± 0.007	0.103 ± 0.007	0.19 ± 0.024	0.019 ± 0.004
Gd	0.0482 ± 0.0124	0.057 ± 0.0102	0.949 ± 0.038	1.47 ± 0.05	1.83 ± 0.06	0.245 ± 0.037	0.577 ± 0.026	0.866 ± 0.082	0.139 ± 0.02
Tb	0.0097 ± 0.002	0.0147 ± 0.0025	0.171 ± 0.007	0.286 ± 0.01	0.38 ± 0.014	0.063 ± 0.008	0.123 ± 0.007	0.177 ± 0.022	0.045 ± 0.007
Dy	0.103 ± 0.0118	0.1213 ± 0.0125	1.46 ± 0.04	2.08 ± 0.05	2.95 ± 0.08	0.734 ± 0.061	0.905 ± 0.036	1.556 ± 0.122	0.24 ± 0.048
Ho	0.0227 ± 0.0035	0.0342 ± 0.0025	0.315 ± 0.01	0.464 ± 0.016	0.615 ± 0.014	0.185 ± 0.016	0.188 ± 0.008	0.296 ± 0.032	0.079 ± 0.011
Er	0.0785 ± 0.0077	0.1514 ± 0.0078	0.805 ± 0.031	1.26 ± 0.04	1.69 ± 0.05	0.595 ± 0.055	0.567 ± 0.032	1.116 ± 0.111	0.253 ± 0.036
Tm	0.014 ± 0.0025	0.0263 ± 0.0032	0.121 ± 0.008	0.166 ± 0.008	0.256 ± 0.009	0.121 ± 0.012	0.079 ± 0.007	0.144 ± 0.016	0.049 ± 0.015
Yb	0.133 ± 0.012	0.1969 ± 0.0194	0.785 ± 0.03	1.11 ± 0.04	1.74 ± 0.06	1.069 ± 0.091	0.506 ± 0.033	0.915 ± 0.091	0.276 ± 0.053
Lu	0.0189 ± 0.0046	0.0285 ± 0.0045	0.115 ± 0.008	0.165 ± 0.009	0.301 ± 0.075	0.149 ± 0.01	0.069 ± 0.006	0.172 ± 0.02	0.03 ± 0.008

	Olivine		Plagioclase				Phosphates[a]		
	Chadacryst	Interstitial							
	SIMS-3	SIMS-8	SIMS-6	SIMS-7	SIMS-14	SIMS-17	LA-ICP-MS		
Y	0.153 ± 0.009	0.19 ± 0.02	0.11 ± 0.008	0.106 ± 0.01	0.128 ± 0.021	0.175 ± 0.027	770.4	842.5	889.5
La	0.0003 ± 0.0003	0.0082 ± 0.0031	0.184 ± 0.008	0.202 ± 0.01	0.297 ± 0.017	0.242 ± 0.019	134.7	163.5	155.4
Ce	0.0006 ± 0.0006	0.0054 ± 0.0037	0.314 ± 0.017	0.343 ± 0.02	0.517 ± 0.033	0.416 ± 0.05	278.8	352.6	353.7
Pr	0.0005 ± 0.0004	0.0015 ± 0.0012	0.036 ± 0.003	0.048 ± 0.006	0.064 ± 0.008	0.055 ± 0.01	42.1	52.4	51.1
Nd	b.d.	b.d.	0.171 ± 0.022	0.141 ± 0.027	0.208 ± 0.044	0.123 ± 0.044	211.1	258.0	247.5
Sm	0.0016 ± 0.0016	0.0098 ± 0.0098	0.035 ± 0.009	0.029 ± 0.008	0.062 ± 0.018	0.045 ± 0.023	78.4	92.5	92.5
Eu	b.d.	0.0021 ± 0.0021	0.511 ± 0.021	0.498 ± 0.021	0.879 ± 0.03	0.693 ± 0.043	21.2	28.4	27.3
Gd	b.d.	0.0054 ± 0.0054	0.025 ± 0.006	0.053 ± 0.012	0.057 ± 0.014	0.052 ± 0.02	117.2	134.3	136.5
Tb	0.0008 ± 0.0004	0.0017 ± 0.0014	0.003 ± 0.001	0.008 ± 0.002	0.005 ± 0.003	0.013 ± 0.005	23.4	26.7	27.4
Dy	0.014 ± 0.004	0.0174 ± 0.0098	0.018 ± 0.004	0.037 ± 0.01	0.02 ± 0.008	0.028 ± 0.013	152.2	169.2	177.6
Ho	0.003 ± 0.001	0.004 ± 0.0019	0.005 ± 0.001	0.01 ± 0.004	0.005 ± 0.003	0.007 ± 0.004	33.2	36.1	38.1
Er	0.0328 ± 0.0055	0.0258 ± 0.0091	0.007 ± 0.003	0.016 ± 0.005	0.016 ± 0.008	0.026 ± 0.015	84.2	91.9	98.7
Tm	0.0069 ± 0.0013	0.0178 ± 0.0047	0.003 ± 0.001	0.002 ± 0.001	b.d.	b.d.	11.8	12.8	13.6
Yb	0.1188 ± 0.0103	0.1002 ± 0.0259	0.005 ± 0.003	0.013 ± 0.006	0.011 ± 0.008	0.013 ± 0.013	72.7	82.7	86.0
Lu	0.0194 ± 0.0027	0.0218 ± 0.0057	0.0004 ± 0.0004	0.001 ± 0.001	0.003 ± 0.002	0.006 ± 0.004	10.2	11.3	12.1

[a]Phosphates were analyzed by LA-ICP-MS with a counting statistics uncertainty (1σ) of <1%.

The arrow shows the analysis direction from the core to the rim of the pigeonite oikocryst with augite mantle.

b.d. = below detection limits.

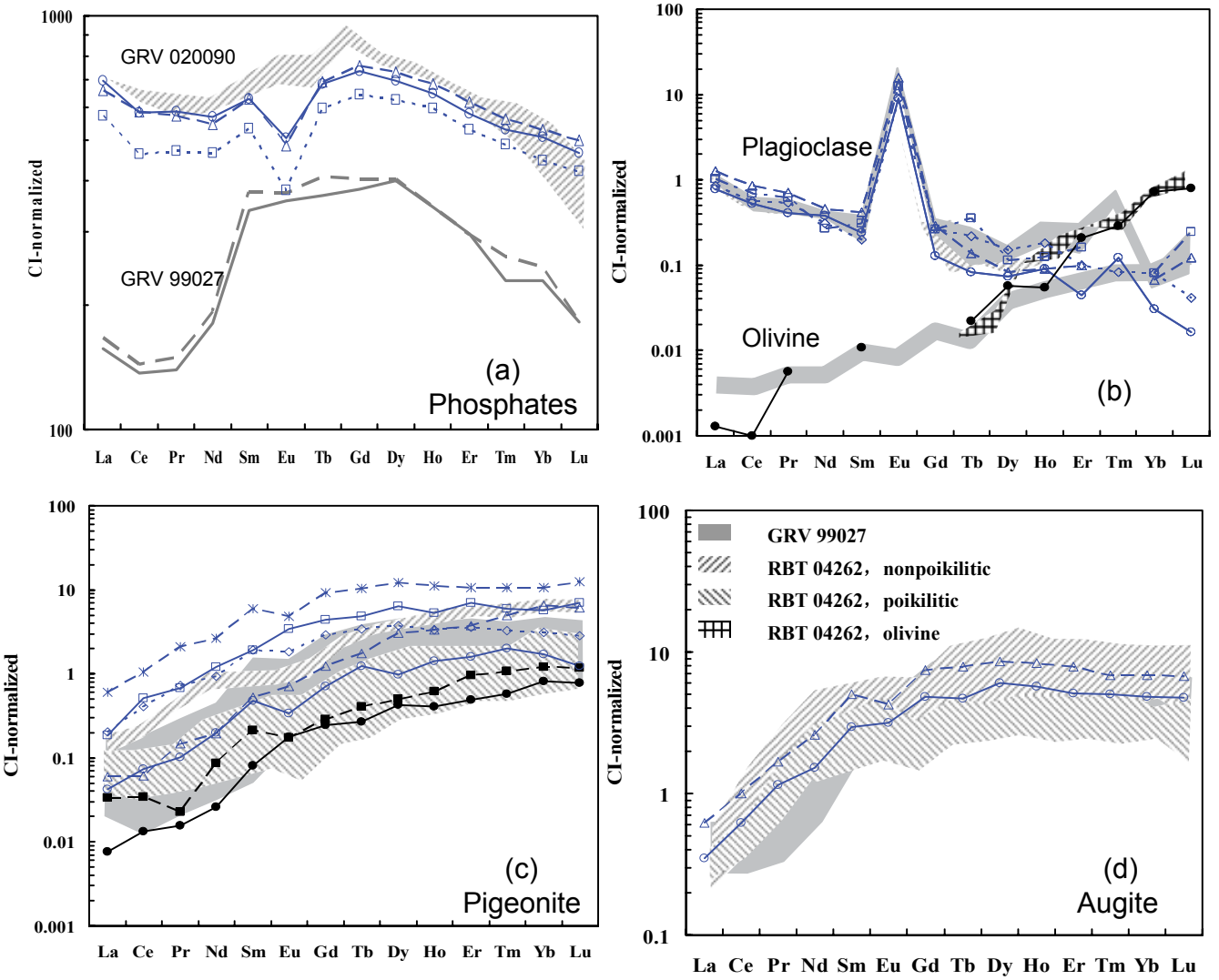

Fig. 9. CI-normalized REE patterns of minerals from GRV 020090. (a) Phosphates contain high REE with significant negative Eu anomaly, but no LREE depletion. (b) Plagioclase shows a relatively constant REE pattern with a positive Eu anomaly. Olivine is highly LREE depleted. (c) Pigeonite shows LREE-depleted patterns with or without negative Eu anomalies. The two analyses of the pigeonite core of the pyroxene oikocryst (filled) have the lowest REE concentrations. (d) Two analyses of the augite mantle of the pyroxene oikocryst, with the more REE-rich analysis closer to the rim. Literature data for GRV 99027 (shaded areas) (Lin et al. 2005) and RBT 04262/1 (hatched areas) (Usui et al. 2010) are shown for comparison.

parent magma, and was included in the subsequently crystallizing olivine. Pigeonite postdated olivine, and grew under stable conditions for a relatively long duration, based on its large grain sizes (up to 6.9 mm). After accumulation of the poikilitic lithology, the intercumulus melt continued to crystallize and formed the nonpoikilitic lithology, with a crystallization sequence of olivine + pigeonite + augite, followed by sulfides, magnetite, baddeleyite + Ti-rich chromite + ilmenite, apatite + merrillite + plagioclases, K-feldspar. In contrast to the poikilitic lithology, which formed at depth, the nonpoikilitic lithology probably crystallized from the intercumulus melt during its ascent to the subsurface, consistent with the smaller grain sizes of this lithology.

Experimental crystallization of low-Ca pyroxene from olivine-phyric shergottite melts under various pressures up to 14.3 kbar has revealed a positive correlation of pressure with the Al/Ti ratios of low-Ca pyroxene (Filiberto et al. 2010). Our analyses of pigeonite in GRV 020090 exhibit a correlation of the Al/Ti ratios with the petrographic settings, i.e., the Al/Ti ratio ranges of the pigeonite oikocrysts are narrow and high, whereas those of the interstitial pigeonite grains are wide and low (Fig. 6b). This observation confirms that the pigeonite oikocrysts precipitated earlier, probably in

the deeper magma chamber, and that the intercumulus melt continuously crystallized to form the nonpoikilitic lithology during its ascent to the subsurface.

Additional lines of evidence for two stages of crystallization lie in the chemical trends of chromite (Fig. 8). As discussed above, the chromite inclusions in the poikilitic lithology are Usp-poor, varying along a line of similar Sp/Usp ratios. In contrast, chromite grains in the nonpoikilitic lithology are Usp-rich, plotting on a line of relatively constant Sp/Chm ratios. The chromite inclusions in the olivine chadacrysts and the pyroxene oikocrysts recorded a trend of increasing the Al_2O_3 and TiO_2 concentrations in the magma chamber due to the precipitation of olivine and pigeonite, with the Cr_2O_3 concentrations buffered by chromite. The Sp contents of the chromite inclusions in the poikilitic lithology increased by a factor of 4.4, from 9.1 mol% up to 40 mol%. This variation requires precipitation of 77 vol% of the magma as cumulus crystals. This is slightly higher than the estimated mode of the poikilitic lithology (43.6 vol%) plus the interstitial olivine (22.5 vol%), although the difference could be due to sampling bias. Another possibility is that the parent magma of GRV 020090 was from the upper part of the magma chamber that had more intercumulus melt and fewer cumulus crystals.

As the melt ascended, the ferromagnesian mafic silicates continued to precipitate, and the intercumulus melt became plagioclase saturated. The Al_2O_3 concentration was buffered by plagioclase. The increased Usp content (from 23.8 to 50.4 mol%) of the interstitial chromite grains reflects the enrichment of TiO_2 in the melt due to precipitation of silicates (olivine, pigeonite, augite, and plagioclase), until the appearance of ilmenite.

The petrography of GRV 020090 is consistent with crystallization of a magma with the bulk composition of this meteorite, calculated with the MELTS program (Ghiorso and Sack 1995; Asimow and Ghiorso 1998). Feldspar and phosphates are the final phases to precipitate, after 78–85% crystallization.

Oxygen fugacities and temperatures of GRV020090 were calculated from chromite-olivine-pigeonite assemblages in the poikilitic lithology and from the chromite-ilmenite assemblages in the nonpoikilitic lithology; the results are listed in Table 7 and plotted in Fig. 10. We note that the oxygen fugacity of GRV 020090 at high temperature overlaps with that of GRV 99027, but it becomes more oxidized than GRV 99027 as temperatures decreased. In Fig. 10, the olivine-chromite-pyroxene assemblages of GRV 020090 plot within the ranges of GRV 99027, whereas the chromite-ilmenite assemblages of GRV 020090 show a marked enhancement of oxygen fugacity relative to the latter. K-feldspar, which occurs at the rims of plagioclase, is

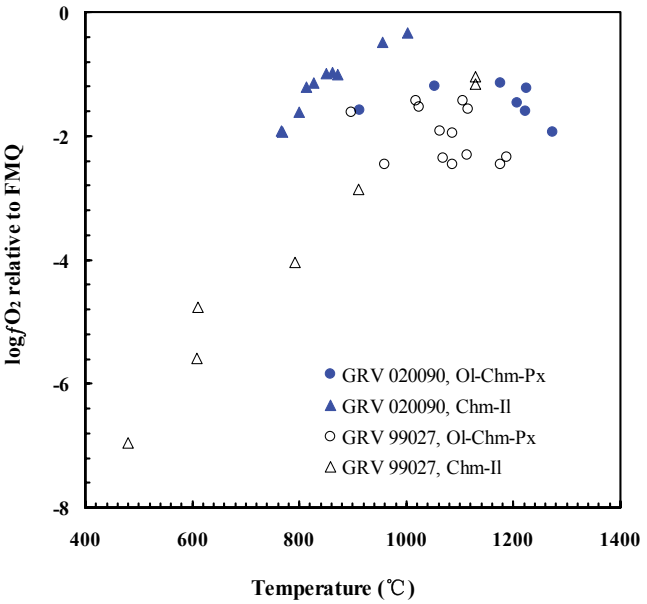

Fig. 10. Oxygen fugacity versus temperature for GRV 020090, calculated with the olivine (Ol), chromite (Chm), pyroxene (Px), and the chromite (Chm)-ilmenite (Il) thermometers and oxygen barometers. GRV 020090 formed under similar redox conditions as GRV 99027, and then evolved to become more oxidized than the latter. Literature data are from Lin et al. (2005). Representative oxygen fugacities and temperatures are listed in Table 7.

representative of the final minerals to crystallize. The equilibrium temperatures between the K-feldspar and plagioclase are 800–850 °C (Fig. 7), consistent with the calculations determined from the chromite-ilmenite assemblages (Fig. 10).

Enriched Upper Mantle Reservoir or Contamination by the Crustal Rocks?

In comparison with other lherzolitic shergottites, GRV020090 has the following specific features: (1) Presence of K-feldspar and a higher abundance of plagioclase that contains more K_2O; (2) Common occurrence of minor baddeleyite; (3) More ferroan compositions of mafic silicates in both lithologies; (4) Higher TiO_2 contents of chromite in the interstitial lithology, but no significant differences for those present in inclusions in the poikilitic lithology; (5) Much higher REE contents of phosphates with LREE enrichment, but similar REE patterns and abundances for the cores of pigeonite oikocrysts and the olivine chadacrysts as those in GRV 99027. These features must be addressed in proposed formation models of GRV 020090.

Fractional Crystallization

During fractional crystallization of a basaltic magma, cumulus crystals (e.g., chromite and olivine

Table 7. Representative compositions of silicates and oxides in GRV 020090 and the calculated temperatures and oxygen fugacities.

	Chm	Px	Ol	Chm	Px	Ol	Chm	Px	Ol	Chm	Il	Chm	Il	Chm	Il
	Poikilitic									Nonpoikilitic					
SiO_2	0.10	54.1	37.6	0.04	53.0	38.1	0.04	53.3	37.5	b.d.	b.d.	b.d.	b.d.	0.02	b.d.
TiO_2	1.58	0.12	0.03	1.37	0.14	0.06	1.87	0.21	0.05	13.5	51.9	16.0	52.1	13.6	53.0
Al_2O_3	8.24	0.45	b.d.	7.48	0.52	0.02	11.8	1.05	b.d.	5.03	0.03	4.25	0.03	4.96	0.04
Cr_2O_3	52.9	0.66	b.d.	54.8	0.31	0.04	45.2	0.52	0.03	24.6	0.47	19.4	0.77	25.7	0.70
FeO	31.1	16.4	28.7	30.7	16.9	26.8	35.1	16.7	31.3	52.8	43.1	57.9	43.3	53.3	42.9
MnO	0.51	0.49	0.50	0.44	0.60	0.56	0.56	0.56	0.55	0.56	0.70	0.62	0.55	0.63	0.72
MgO	5.37	24.3	34.1	5.29	24.6	35.1	3.34	20.9	32.0	2.62	3.70	2.25	3.49	2.49	3.54
CaO	b.d.	3.78	0.08	b.d.	2.83	0.10	b.d.	6.91	0.15	b.d.	0.29	b.d.	0.03	b.d.	b.d.
Na_2O	b.d.	0.09	0.03	0.04	0.11	b.d.	0.06	0.18	b.d.	b.d.	0.02	b.d.	b.d.	b.d.	b.d.
K_2O	0.02	0.01	0.01	b.d.	0.01	b.d.	b.d.	0.01	0.01	b.d.	b.d.	0.01	b.d.	b.d.	b.d.
Total	99.88	100.49	101.02	100.17	98.97	100.80	98.03	100.42	101.53	99.10	100.13	100.54	100.24	100.65	100.91
Chm	71.9			74.5			62.3			34.7		27.2		35.8	
Sp	16.7			15.2			24.2			10.6		8.9		10.3	
Mt	7.1			6.8			8.6			18.6		21.4		18.0	
Usp	4.1			3.5			4.9			36.1		42.6		35.9	
fe#	0.732			0.734			0.831			0.896		0.915		0.902	
Cr#	0.812			0.831			0.720			0.766		0.754		0.777	
T(°)	1222			1176			912			956		827		767	
$\log fO_2$	−1.6			−1.1			−1.6			−0.5		−1.2		−1.9	

fe# = $Fe^{2+}/[Fe^{2+}+Mg]$; Cr#: Cr/[Cr+Al]; b.d. = below detection limit; $\log fO_2$ = The oxygen fugacities are relative to the QFM buffer.
Chromite-olivine-pigeonite thermometer and oxygen barometer are after Sack and Ghiorso (1991) and Wood (1991), respectively.
Chromite-ilmenite thermometer and oxygen barometer are after Ghiorso and Sack (1991).

chadacrysts and pyroxene oikocrysts) settle to the bottom of the magma chamber, and the residual melt evolves to be enriched in FeO, SiO_2, Al_2O_3, and incompatible trace elements (ITE). Mikouchi et al. (2008) proposed that various lherzolitic shergottites were probably derived from different stratigraphic units of the same lherzolitic shergottite igneous block, with RBT 04262 from the upper part and GRV 99027 and ALHA77005 from the lower part. This model can explain many of the observed variations among lherzolitic shergottites, including their modal compositions, FeO contents of olivine and pyroxenes, and TiO_2 contents of chromite in the interstitial lithology. TiO_2-poor compositions of chromite inclusions in poikilitic lithology are also expected in this scenario. However, fractional crystallization of a lherzolitic shergottitic magma will merely enhance the concentrations of REE in the residual melt without significantly changing the REE patterns. This has been demonstrated by the nearly parallel REE patterns of the bulk meteorite and the melts in equilibrium with minerals of GRV 99027 (Lin et al. 2005) and LEW 88516 (Harvey et al. 1993). The very high REE concentrations and especially the LREE-enriched patterns of phosphates in GRV 020090 (Fig. 9a) and RBT 04262/1 (Usui et al. 2010) are, therefore, not likely to be derived from a LREE-depleted magma by a fractional crystallization process. Figure 11 shows the REE pattern of bulk GRV 020090 calculated from the modal composition (Table 1) and the averages of the REE analyses (Table 6), which is clearly different from that of the magma in equilibrium with the core of the pigeonite oikocryst. Furthermore, as the REE concentrations of the melts increase, the REE patterns evolve from significantly LREE depleted to non-LREE depleted. This observation can be explained by assimilation of geochemically enriched Martian crustal materials as the melt ascended to the subsurface.

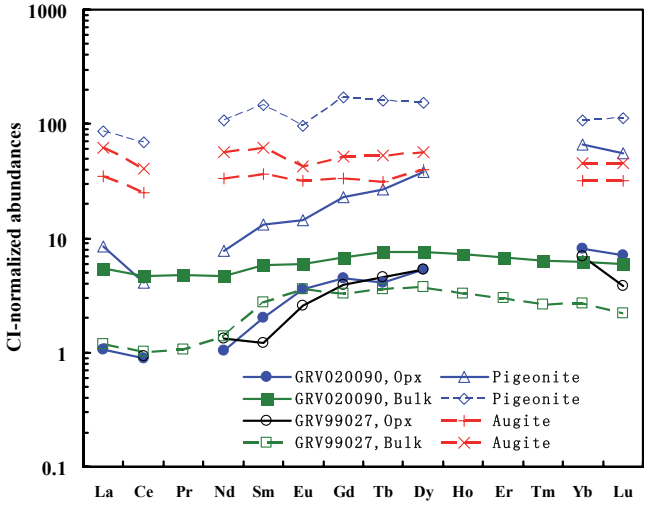

Fig. 11. Calculated REE patterns for the bulk rock and for melts in equilibrium with minerals from GRV 020090. The melt in equilibrium with the core of the pigeonite oikocryst (Opx) shows a LREE-depleted pattern, different from the nearly flat REE pattern of the bulk meteorite. As the concentrations of REE increase, the residual melt changed from LREE depleted to non-LREE depleted. The literature data are from Lin et al. (2005); REE partition coefficients are from Norman (1999).

Enriched Upper Mantle Reservoir

The oxidized and enriched features of GRV 020090 are expected for a parental magma derived from a geochemically enriched Martian upper mantle reservoir. This scenario has been proposed for the enriched basaltic shergottites (e.g., Herd et al. 2002; Herd 2003; Bridges and Warren 2006). A critical line of evidence for the origin of RBT 04262 from a geochemically enriched reservoir is the high initial $^{87}Sr/^{86}Sr$ ratio (0.722745 ± 19) and low initial ε_{Nd} value (−6.7 ± 0.2) (Shih et al. 2009), clearly distinct from the depleted Martian upper mantle, but close to that of the enriched basaltic shergottites. However, the LREE-depleted pattern of the primordial parent magma of GRV 020090, calculated from the REE abundance of the core of the pigeonite oikocryst, is inconsistent with such an enriched reservoir (Fig. 11). In fact, the REE patterns of the primordial magmas of both GRV 020090 and GRV 99027 are nearly identical (Fig. 11). Although the REE abundances of the olivine chadacrysts are slightly higher in GRV 020090 than in GRV99027, the former do not show any sign of LREE enrichment (Fig. 9b), also inconsistent with the enriched reservoir hypothesis. Another indication of the similar parent magma compositions of GRV 020090 and GRV 99027 is the nearly identical chemistry of chromite inclusions in the olivine chadacrysts and pigeonite oikocrysts between both meteorites. These observations argue against an origin of GRV 020090 from an enriched reservoir, but suggest similar parent magmas for GRV 020090 and GRV 99027.

Contamination by Oxidized and Enriched Martian Crust

Fractional crystallization of a primordial magma followed by assimilation of oxidized and enriched crustal materials during its intrusion into the subsurface is consistent with our observations and the two-stage model discussed above. The parent magma of GRV 020090 was probably derived from the upper layer of a magma chamber that had more crystals accumulated at the bottom. Crystallization of such an evolved parent magma would result in a higher abundance of plagioclase and more ferroan compositions of olivine

and pyroxenes as indicated by the observations of GRV 020090. However, the enriched features of GRV 020090 are probably secondary.

A late LREE enrichment of the magma of GRV020090 is revealed by the trace element analyses of the minerals. The cores of olivine chadacrysts represent the earliest silicate precipitating from the parent magma. Our REE analyses of the cores of the olivine chadacrysts from GRV 020090 show a more LREE-depleted pattern than that of GRV 99027 and other lherzolitic shergottites (Fig. 9b). The La and Ce concentrations are approximately 0.001 × CI in GRV 020090, in comparison to approximately 0.004 × CI in GRV 99027 (Lin et al. 2005) and 0.005–0.02 × CI in ALHA77005 (Lundberg et al. 1990). The LREE depletion of the parent magma of GRV 020090 is confirmed by the low REE abundances of the cores of the pigeonite oikocrysts that crystallized after the olivine chadacrysts (Fig. 9c). The lowest concentrations of La (0.007 × CI) and Ce (0.013 × CI) in the pigeonite oikocrysts in GRV 020090 are similar to, or even lower than, those in GRV 99027 (La: 0.023 × CI, Ce: 0.014 × CI) (Lin et al. 2005). In comparison, the cores of orthopyroxene in the depleted olivine-phyric basaltic shergottite Yamato 980459 contain higher La (0.02 × CI) and Ce (0.06 × CI) (Usui et al. 2008). The LREE depletions of the olivine chadacrysts and pigeonite oikocryst are robust evidence against the origin of GRV 020090 from an enriched reservoir.

Contamination of the magma by oxidized and enriched crustal materials postdated the poikilitic lithology and probably the appearance of augite and plagioclase. The lowest REE abundances of the augite rims of the pyroxene oikocrysts in GRV 020090 (La: 0.32 × CI, Ce: 0.49 × CI) are comparable with those in GRV 99027 (La: 0.26 × CI, Ce: 0.25 × CI) (Lin et al. 2005), and the lowest REE concentrations of plagioclase (La: 0.78 × CI, Ce: 0.57 × CI) are nearly the same as those in GRV 99027 (La: 0.98 × CI; Ce: 0.44 × CI). The REE abundances of pigeonite and augite show wide variations, but with nearly parallel patterns (Fig. 9c), and reflect the increase in REE concentrations of the melt with crystallization, without significant fractionation of REEs. The nearly parallel variation in REE abundances in pyroxenes was also found in the GRV 99027 (Lin et al. 2005), ALHA77005 (Lundberg et al. 1990), and RBT 04262/1 (Usui et al. 2010).

Another line of evidence for assimilation of Martian crustal materials is a positive correlation between the water contents and δD values of apatite in GRV 020090, which has been explained as the combined effects of fractional crystallization and addition of D-enriched water via assimilation of Martian crustal materials (Hu et al. 2012). The increased oxygen fugacity when ilmenite precipitated from the residual melt of GRV 020090 (Fig. 10), compared with the monotonic decrease seen in GRV 99027, is also consistent with addition of oxidized Martian crustal materials.

Formation Model of GRV 020090

Based on the above discussion, the formation of GRV 020090 can be summarized in terms of a two-stage model. Following the formation of a magma chamber first derived from partial melting of Martian upper mantle, minerals, in order of chromite, olivine, and pigeonite, crystallized from the magma and accumulated to the bottom of the chamber, resulting in a stratified magma chamber. The upper layer of the magma chamber, which was more ferroan in chemical composition and had fewer cumulus crystals, but more intercumulus melt relative to the whole magma chamber, is considered to be the parent magma of GRV020090. However, this primordial parent magma of GRV 020090 was not geochemically enriched as indicated by the low REE abundances of the cumulus crystals, which are similar to those in GRV 99027 and other depleted or moderately depleted lherzolitic shergottites.

As the magma ascended to the subsurface of Mars, the intercumulus melt continuously crystallized to form the nonpoikilitic lithology. During this period, the melt was probably contaminated by oxidized and enriched crustal materials. In addition to the high oxygen fugacity recorded by oxides, phosphates crystallized from this contaminated melt show a characteristic LREE enrichment that is distinct from what is observed in GRV 99027 and other moderately depleted lherzolitic shergottites.

CONCLUSIONS

GRV 020090 shares the typical textures and mineral chemistry of lherzolitic shergottites, and can, therefore, be classified as a new member of this subgroup. However, differences between GRV 020090 and other lherzolitic shergottites (except for RBT 04262/04261) are significant. GRV 020090 contains a high abundance of plagioclase, presence of K-feldspar, common occurrence of baddeleyite, ferroan compositions of olivine and pyroxenes, Ti-enrichment of the interstitial chromite, and LREE enrichment of phosphates. GRV 020090, like RBT 04262/04261, can be referred to as an enriched lherzolitic shergottite.

We propose that the parent magma of GRV 020090 was derived from the upper layer of a stratigraphic magma produced by partial melting of the Martian upper

mantle. The parent magma contained fewer cumulus crystals and had a more ferroan composition than the whole magma chamber. The nonpoikilitic lithology of GRV 020090 was formed from the intercumulus melt, which was contaminated by the crustal materials, as it ascended to the subsurface of Mars. GRV 020090 and RBT 04262 may have sampled a region on Mars different from that of other lherzolitic shergottites.

Acknowledgments—The authors are grateful to Drs. Filiberto and Herd and an anonymous reviewer for their constructive reviews, and to the AE, Dr. Floss, for her helpful suggestions and editorial corrections. The sample was provided by the Polar Research Institute of China, and this study was supported by the Knowledge Innovation Program (KZCX2-YW-Q08) and the Natural Science Foundation of China (Grant No. 40830421, 41273077).

Editorial Handling—Dr. Christine Floss

REFERENCES

Anand M., James S., Greenwood R. C., Johnson D., Franchi I. A., and Grady M. M. 2008. Mineralogy and geochemistry of shergottite RBT 04262 (abstract #2173). 39th Lunar and Planetary Science Conference. CD-ROM.

Asimow P. D. and Ghiorso M. S. 1998. Algorithmic modifications extending MELTS to calculate subsolidus phase relations. *American Mineralogist* 83:1127–1131.

Borg L. E., Nyquist L. E., Wiesmann H., and Reese Y. 2002. Constraints on the petrogenesis of Martian meteorites from the Rb-Sr and Sm-Nd isotopic systematics of the lherzolitic shergottites ALH77005 and LEW88516. *Geochimica et Cosmochimica Acta* 66:2037–2053.

Bridges J. C. and Warren P. H. 2006. The SNC meteorites: Basaltic igneous processes on Mars. *Journal of the Geological Society* 163:229–251.

Bunch T. W., Irving A. J., Wittke J. H., and Kuehner S. M. 2005. NWA 2646: A Martian plagioclase-olivine clinopyroxenite akin to "lherzolitic shergottites" (abstract). *Meteoritics & Planetary Science* 40:A25.

Ebihara M., Kong P., and Shinotsuka K. 1997. Chemical composition of Y-793605, a Martian lherzolite. *Antarctic Meteorite Research* 10:83–94.

Eugster O., Busemann H., Lorenzetti S., and Terribilini D. 2002. Ejection ages from krypton-81—krypton-83 dating and pre-atmospheric sizes of Martian meteorites. *Meteoritics & Planetary Science* 37:1345–1360.

Filiberto J., Musselwhite D. S., Gross J., Burgess K., Le L., and Treiman A. H. 2010. Experimental petrology, crystallization history, and parental magma characteristics of olivine-phyric shergottite NWA 1068: Implications for the petrogenesis of "enriched" olivine-phyric shergottites. *Meteoritics & Planetary Science* 45:1258–1270.

Ghiorso M. S. and Sack R. O. 1991. Fe-Ti oxide geothermometry: Thermodynamic formulation and the estimation of intensive variables in silicic magmas. *Contributions to Mineralogy and Petrology* 108:485–510.

Ghiorso M. S. and Sack R. O. 1995. Chemical mass transfer in magmatic processes IV: A revised and internally consistent thermodynamic model for the interpretation and extrapolation of liquid solid equilibria in magmatic systems at elevated temperatures and pressures. *Contributions to Mineralogy and Petrology* 119:197–212.

Gillet P., Barrat J. A., Beck P., Marty B., Greenwood R. C., Franchi I. A., Bohn M., and Cotten J. 2005. Petrology, geochemistry, and cosmic-ray exposure age of lherzolitic shergottite Northwest Africa 1950. *Meteoritics & Planetary Science* 40:1175–1184.

Harvey R. P., Wadhwa M., McSween H. Y. J., and Crozaz G. 1993. Petrography, mineral chemistry and petrogenesis of Antarctic shergottite LEW 88516. *Geochimica et Cosmochimica Acta* 57:4769–4783.

Herd C. D. K. 2003. The oxygen fugacity of olivine-phyric Martian basalts and the components within the mantle and crust of Mars. *Meteoritics & Planetary Science* 38:1793–1805.

Herd C. D. K., Borg L. E., Jones J. H., and Papike J. J. 2002. Oxygen fugacity and geochemical variations in the Martian basalts: Implications for Martian basalt petrogenesis and the oxidation state of the upper mantle of Mars. *Geochimica et Cosmochimica Acta* 66:2025–2036.

Hu S., Feng L., and Lin Y. 2011. Petrography, mineral chemistry and shock metamorphism of Yamato 984028 lherzolitic shergottite. *Chinese Science Bulletin* 56:1579–1587.

Hu S., Lin Y. T., Zhang J. C., Hao J. L., Feng L., Yang W., Zhao X. C. 2012. Hydrogen isotopic evidence for liquid water on Mars and constraints on Martian magmatic and meteoric water (abstract #5101). 75th Annual Meeting of the Meteoritical Society.

Ikeda Y. 1997. Petrology and mineralogy of the Y-793605 Martian meteorite. *Antarctic Meteorite Research* 10:13–40.

Irving A. J., Kuehner S. M., Korotev R. L., and Hupé G. M. 2007. Petrology and bulk composition of primitive enriched olivine basaltic shergottite Northwest Africa 4468 (abstract #1526). 38th Lunar and Planetary Science Conference. CD-ROM.

Irving S., Bunch T., Kuehner S., Korotev R., and Classen N. 2008. Unique ultramafic shergottite Northwest Africa 4797: A highly shocked Martian wehrlite cumulation related to enriched basaltic (not "lherzolitic") (abstract #1391). 39th Lunar and Planetary Science Conference. CD-ROM.

Jiang Y. and Hsu W. 2012. Petrogenesis of Grove Mountains 020090: An enriched "lherzolitic" shergottite. *Meteoritics & Planetary Science* 47:1–17.

Kong P., Fabel D., Brown R., and Freeman S. 2007. Cosmic-ray exposure age of Martian meteorite GRV 99027. *Science in China Series D: Earth Sciences* 50:1521–1524.

Lin Y., Wang D., Miao B., Ouyang Z., Liu X., and Ju Y. 2003. Grove Mountains (GRV) 99027: A new Martian meteorite. *Chinese Science Bulletin* 48:1771–1774.

Lin Y., Guan Y., Wang D., Kimura M., and Leshin L. A. 2005. Petrogenesis of the new lherzolitic shergottite Grove Mountains 99027: Constraints of petrography, mineral chemistry, and rare earth elements. *Meteoritics & Planetary Science* 40:1599–1619.

Lin Y., Qi L., Wang G., and Xu L. 2008a. Bulk chemical composition of lherzolitic shergottite Grove Mountains (GRV) 99027—Constraints on the mantle of Mars. *Meteoritics & Planetary Science* 43:1179–1187.

Lin Y., Liu T., Shen W., Xu L., and Miao B. 2008b. Grove Mountains (GRV) 020090: A highly fractionated

lherzolitic shergottite (abstract). *Meteoritics & Planetary Science* 43:A86.

Liu T., Li C., and Lin Y. 2011. Rb-Sr and Sm-Nd isotopic systematics of the lherzolitic shergottite GRV 99027. *Meteoritics & Planetary Science* 46:681–689.

Lundberg L. L., Crozaz G., and McSween H. Y., Jr. 1990. Rare earth elements in minerals of the ALHA77005 shergottite and implications for its parent magma and crystallization history. *Geochimica et Cosmochimica Acta* 54:2535–2547.

Miao B., Ouyang Z., Wang D., Ju Y., Wang G., and Lin Y. 2004. A new Martian meteorite from Antarctica: Grove Mountains (GRV) 020090. *Acta Geologica Sinica* 78:1034–1041.

Mikouchi T. and Kurihara T. 2008. Mineralogy and petrology of paired lherzolitic shergottites Yamato 000027, Yamato 000047, and Yamato 000097: Another fragment from a Martian "lherzolite" block. *Polar Science* 2:175–194.

Mikouchi T. and Miyamoto M. 1997. Yamato-793605: A new lherzolitic shergottite from the Japanese Antarctic meteorite collection. *Antarctic Meteorite Research* 10:41–60.

Mikouchi T., Kurihara T., and Miyamoto M. 2008. Petrology and mineralogy of RBT 04262: Implications for stratigraphy of the lherzolitic shergottite igneous block (abstract #2403). 39th Lunar and Planetary Science Conference. CD-ROM.

Niihara T. 2011. Uranium-lead age of baddeleyite in shergottite Roberts Massif 04261: Implications for magmatic activity on Mars. *Journal Geophysical Research* 116:E12008.

Norman M. D. 1999. The composition and thickness of the crust of Mars estimated from REE and Nd isotopic compositions of Martian meteorites. *Meteoritics & Planetary Science* 34:439–449.

Nyquist L. E., Bogard D. D., Shih C.-Y., Greshake A., Stoeffler D., and Eugster O. 2001. Ages and geologic histories of Martian meteorites. *Space Science Reviews* 96:105–164.

Presnall D. C. 1995. Phase diagrams of Earth-forming minerals. In *Mineral physics and crystallography: A handbook of physical constants*, edited by Ahrens T. J. Washington, D.C.: American Geophysical Union. pp. 248–268.

Riches A. J. V., Liu Y., Day J. M. D., Puchtel I. S., Rumble Iii D., McSween H. Y., Jr., Walker R. J., and Taylor L. A. 2011. Petrology and geochemistry of Yamato 984028: A cumulate lherzolitic shergottite with affinities to Y 000027, Y 000047, and Y 000097. *Polar Science* 4:497–514.

Sack R. O. and Ghiorso M. S. 1991. Chromian spinels as petrogenetic indicators: Thermodynamics and petrologic applications. *American Mineralogist* 76:827–847.

Shearer C. K., Burger P. V., Papike J. J., Borg L. E., Irving A. J., and Herd C. 2008. Petrogenetic linkages among Martian basalts: Implications based on trace element chemistry of olivine. *Meteoritics & Planetary Science* 43: 1241–1258.

Shih C.-Y., Nyquist L. E., and Reese Y. 2009. Rb-Sr and Sm-Nd studies of olivine-phyric shergottites RBT 04262 and LAR 06319: Isotopic evidence for relationship to enriched basaltic shergottites (abstract #1360). 40th Lunar and Planetary Science Conference. CD-ROM.

Treiman A. H., McKay G. A., Bogard D. D., Mittlefehldt D. W., Wang M. S., Keller L., Lipschutz M. E., Lindstrom M. M., and Garrison D. 1994. Comparison of the LEW88516 and ALHA77005 Martian meteorites: Similar but distinct. *Meteoritics* 29:581–592.

Usui T., McSween H. Y., Jr., and Floss C. 2008. Petrogenesis of olivine-phyric shergottite Yamato 980459, revisited. *Geochimica et Cosmochimica Acta* 72:1711–1730.

Usui T., Sanborn M., Wadhwa M., and McSween H. Y., Jr. 2010. Petrology and trace element geochemistry of Robert Massif 04261 and 04262 meteorites, the first examples of geochemically enriched lherzolitic shergottites. *Geochimica et Cosmochimica Acta* 74:7283–7306.

Wadhwa M., McKay G. A., and Crozaz G. 1999. Trace element distributions in Yamato-793605, a chip off the "Martian lherzolite" block. *Antarctic Meteorite Research* 12:168–182.

Warren P. H. and Kallemeyn G. W. 1997. Yamato-793605, EET79001, and other presumed Martian meteorites: Compositional clues to their origins. *Antarctic Meteorite Research* 10:61–81.

Wood B. J. 1991. Oxygen barometry of spinel peridotites. In *Oxide minerals: Petrologic and magnetic significance*, edited by Lindsley D. H. Reviews in mineralogy, vol. 25. Washington, D.C.: Mineralogical Society of America. pp. 417–431.